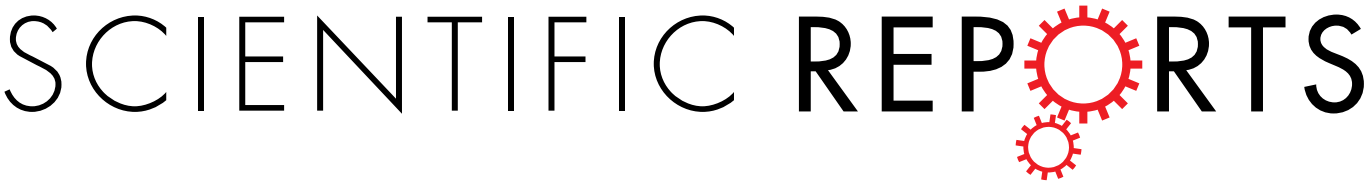

OPEN

Holey graphene frameworks for highly selective post-combustion carbon capture

Received: 09 December 2015
Accepted: 27 January 2016
Published: 16 February 2016

Shamik Chowdhury & Rajasekhar Balasubramanian

Atmospheric CO_2 concentrations continue to rise rapidly in response to increased combustion of fossil fuels, contributing to global climate change. In order to mitigate the effects of global warming, development of new materials for cost-effective and energy-efficient CO_2 capture is critically important. Graphene-based porous materials are an emerging class of solid adsorbents for selectively removing CO_2 from flue gases. Herein, we report a simple and scalable approach to produce three-dimensional holey graphene frameworks with tunable porosity and pore geometry, and demonstrate their application as high-performance CO_2 adsorbents. These holey graphene macrostructures exhibit a significantly improved specific surface area and pore volume compared to their pristine counterparts, and can be effectively used in post-combustion CO_2 adsorption systems because of their intrinsic hydrophobicity together with good gravimetric storage capacities, rapid removal capabilities, superior cycling stabilities, and moderate initial isosteric heats. In addition, an exceptionally high CO_2 over N_2 selectivity can be achieved under conditions relevant to capture from the dry exhaust gas stream of a coal burning power plant, suggesting the possibility of recovering highly pure CO_2 for long-term sequestration and/or utilization for downstream applications.

The global annual mean concentration of CO_2 in the atmosphere has increased markedly from pre-industrial levels of about 280 parts per million (ppm) to 400 ppm in 2013[1]. Further increases are expected as the annual burning of fossil fuels is likely to continue to rise rapidly to meet the spiraling energy demand of an escalating human population. A massive effort must be undertaken to reduce the amount of CO_2 entering the atmosphere because of its contribution to global climate change[2]. There is a widespread consensus that the development and deployment of a broad portfolio of advanced energy technologies would be the most effective and sustainable approach to bring about stabilization of the atmospheric CO_2 concentrations[1]. While energy efficiency improvements and increased use of renewable energy resources are a long-term proposition of this portfolio[3], carbon capture, utilization and storage (CCUS) is a short to medium term technological option for mitigating anthropogenic energy-related CO_2 emissions[4–6]. Of the various strategies (i.e., pre-combustion, post-combustion and oxy-fuel combustion) and numerous technologies (e.g., absorption, adsorption, membrane separation and cryogenic distillation) that are currently being explored to capture CO_2 from fossil-fuelled power plants and other large industrial sources[1,7], post-combustion capture using porous adsorbents constitutes a promising solution because of its simplicity and cost effeciency[8]. A variety of porous solids have been extensively investigated among which porous carbons are particularly well-suited to be deployed within post-combustion CO_2 capture systems, owing to their abundant porosity and ease of fabrication[8].

Three-dimensional (3D) graphene-based frameworks (3D-GFs) such as aerogels, hydrogels, foams, sponges, and nanomesh are an important new class of porous carbon materials, attracting increasing attention for energy-related applications[9,10]. Due to their unique continuously interconnected networks, 3D-GFs exhibit large accessible surface area, high pore volume, excellent stability, good flexibility, and adequate mechanical strength[11,12]. As such, these materials can also serve as robust adsorbents for capturing CO_2 emanating from the combustion of fossil fuels. For example, a graphene hydrogel, made from the self-assembly of graphene oxide sheets *via* a hydrothermal process, had a 3D porous structure, high specific surface area ($530\ m^2\ g^{-1}$) and large pore volume ($0.66\ cm^3\ g^{-1}$), and consequently showed great promise for CO_2 adsorption and separation applications[13]. However, such 3D-GFs generally lack well-defined mesopores and/or micropores[9], which can

Department of Civil & Environmental Engineering, National University of Singapore, 1 Engineering Drive 2, Singapore 117576, Republic of Singapore. Correspondence and requests for materials should be addressed to R.B. (email: ceerbala@nus.edu.sg)

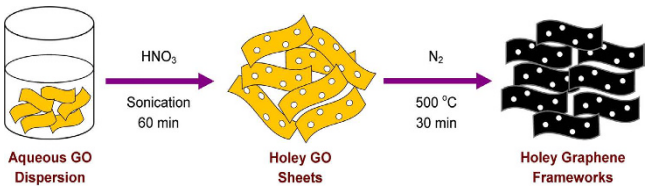

Figure 1. Illustration of the major steps involved in the preparation of HGFs. The synthesis involves etching of in-plane nanopores into GO sheets and their self-assembly into a 3D interconnected network structure.

substantially limit the efficiency of mass transport and gas diffusion through the pore networks. Therefore, it is highly desirable to develop hierarchical porous 3D-GFs by integrating holey graphene nanosheets into a macroscopic 3D interconnected network structure.

Here, we describe a facile and scalable approach to produce holey graphene frameworks (HGFs) by etching in-plane nanopores into graphene sheets through a wet chemical method, that allows a tunable pore geometry and controllable pore density, followed by their self-assembly to form a 3D interconnected porous macrostructure. The as-synthesized HGFs were found to have high specific surface area and large pore volume with well-developed mesoporosity. We further show that these HGFs are extremely attractive for post-combustion CO_2 adsorption applications, including good gravimetric capacity, rapid removal capability, superior cycling stability, and moderate initial isosteric heat of adsorption. Most importantly, the CO_2 over N_2 adsorption selectivity is among the highest at operating conditions pertinent to post-combustion capture from coal-fired power plants, which would indeed be extremely beneficial for extracting a high-purity CO_2 stream from flue gases for deep underground storage or other industrial applications.

Results

Preparation and characterization of HGFs. Figure 1 presents a schematic of the methodology adopted for preparing HGFs. A homogenous aqueous dispersion of graphene oxide (GO) was mixed with a desired amount of 69 wt.% concentrated HNO_3 under stirring. The mixture was then subjected to sonication in a water bath at sufficient acoustic pressure and room temperature for 1 h. After removing the residual HNO_3 by centrifuging and washing the reaction mixture, the as-obtained holey graphene oxide (HGO) was annealed under N_2 atmosphere at 500 °C for 30 min in a horizontal tube furnace. During the thermal annealing process, the HGO sheets were reduced and self-assembled to form 3D HGF. Three different solutions of increasing HNO_3 concentrations were tested, corresponding to a GO suspension/HNO_3 volume ratio of 1/3 (mL/mL) (I), 1/6 (mL/mL) (II) and 1/9 (mL/mL) (III). The resulting HGF were labeled as HGF-I, HGF-II and HGF-III, respectively. For comparison, we also synthesized non-holey GFs (NGFs) using the same procedure but without any acid treatment. Compared to the template-assisted chemical vapor deposition (CVD) method, the current synthesis method is simpler and economically more attractive, making the process readily scalable for large scale production of porous graphene materials.

The wide-angle X-ray diffraction (XRD) patterns of all the HGFs were very similar to those of typical sp^2-bonded carbons, exhibiting the development of crystalline graphene structure (Fig. 2a). The characteristic GO peak at $2\theta = 11°$ was absent in all the samples. Instead, two strong and broad peaks were observed at around $2\theta = 25°$ and 43.3°, conforming to the graphitic (0 0 2) and (1 0 0) crystal planes, respectively. In accordance with the XRD results, the X-ray photoelectron spectroscopy (XPS) survey scan of the HGFs indicated that GO was sufficiently reduced by thermal annealing at 500 °C, with a significant deoxygenation during the acid etching process (Fig. 2b) (see Supplementary Fig. 1 for the XPS survey scans of HGOs). The reduction of oxygenated functional groups was also confirmed by Fourier transform infrared (FTIR) spectroscopy, as shown in Supplementary Fig. 2.

Further structural information about the prepared HGFs was obtained from Raman spectroscopy. All the samples without exception showed three prominent absorption bands at about 1350 and 1596 cm^{-1}, which correspond to the well-documented D (related to defect in sp^2 lattice) and G (related to pristine sp^2 graphitic layer) bands, respectively (Fig. 2c)[14–16]. The D/G intensity ratios of the HGFs ($I_D/I_G = 1.09$ for HGF-I, 1.20 for HGF-II, and 1.26 for HGF-III) were found to be larger than that of GO ($I_D/I_G = 0.77$), and are in agreement with the literature[17]. In contrast to the Raman spectrum of NGF ($I_D/I_G = 1.02$) obtained without acid sonication, the remarkably strong D band intensity for the HGF samples could be ascribed to the introduction of in-plane carbon vacancy defects (pores) during the etching of GO with HNO_3. Because the sp^3 carbon atoms are chemically more active than the sp^2 carbons in the bulk of GO[18,19], HNO_3 molecules mainly attack the oxygenic defect regions, leading to the preferential removal of oxygenated carbon atoms and generation of carbon vacancies that gradually extend into nanopores[19]. The role of oxygenated carbon species in the formation and evolution of pores is corroborated by the large difference between the O/C atomic ratios of GO (atomic O/C = 0.46) and HGOs (atomic O/C = 0.32, 0.24 and 0.17 for HGO-I, HGO-II and HGO-III, respectively) calculated from their XPS survey scans (Fig. 2b and Supplementary Fig. 1). Additionally, as the defective carbon sites are usually distributed throughout the basal plane of GO[20], the etching process could occur across the entire graphene sheets to result in abundant in-plane pores of a few nanometres all over the sheet[21]. However, excessive HNO_3 would lead to a more aggressive etching, enlarging the pore size of holey graphene, as inferred from the increase in the I_D/I_G ratio with increasing etchant concentration.

The porous morphology of the samples was confirmed by field emission scanning electron microscopy (FESEM) and transmission electron microscopy (TEM). From the FESEM micrographs of the HGFs (Fig. 3a

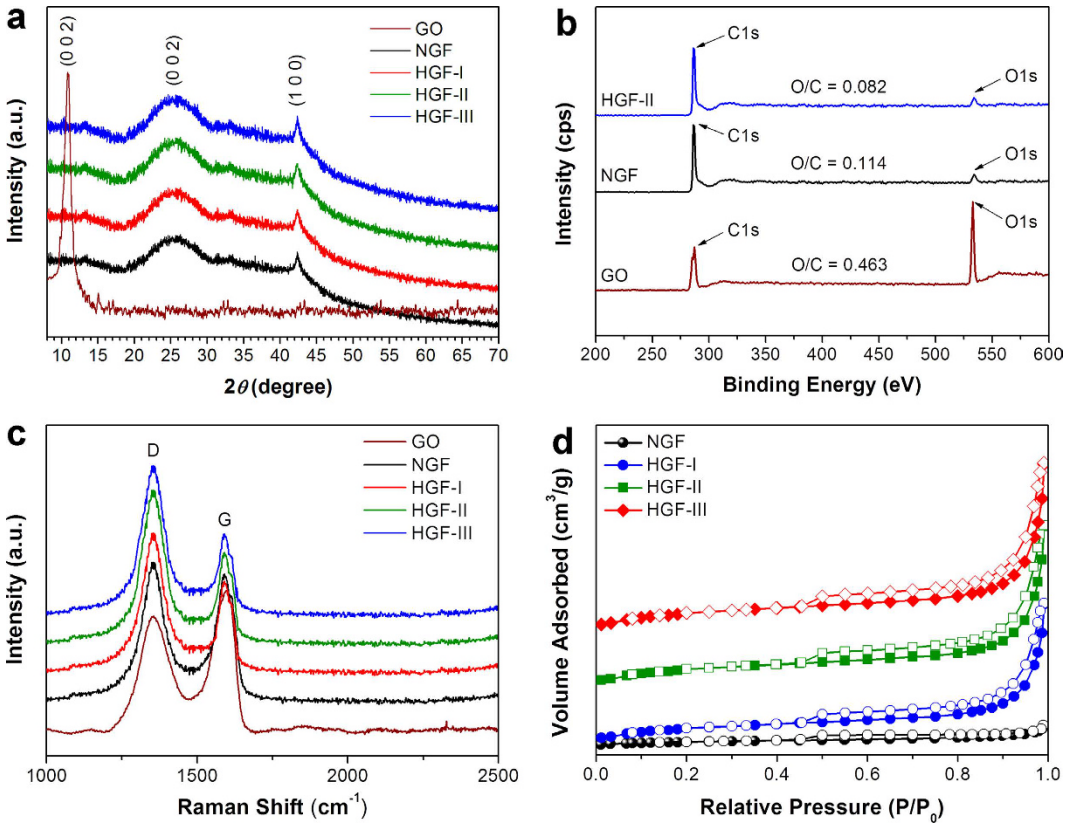

Figure 2. Structural characterization of HGFs. (**a**) Wide angle XRD patterns, (**b**) XPS survey spectra, (**c**) Raman spectra and (**d**) N_2 adsorption/desorption isotherms of GO, NGF, and HGFs. The solid and open symbols represent adsorption and desorption, respectively.

and Supplementary Fig. 3), a distinct 3D porous framework consisting of interconnected networks of randomly oriented sheet-like structures was clearly observed. These sheets were rather thin and wrinkled as revealed by low-magnification TEM (Fig. 3c,d), indicating the efficient self-assembling of 2D porous graphene nanosheets into 3D macrostructures through a combination of hydrophobic and π−π interactions[22,23]. The NGF, on the other hand, displayed a planar but contorted structure (Fig. 3b), ascertaining the involvement of HNO_3 molecules in pore development, and thus the change in morphological appearance of the graphene layers.

To assess the pore structures of the developed graphene frameworks, the N_2 adsorption/desorption isotherms were measured. All the samples generated a type IV isotherm with a type H3 hysteresis loop in the relative pressure region of 0.45–1.0 (Fig. 2d), often associated with non-rigid aggregates of plate-like particles forming slit-shaped mesopores[24]. The calculated Brunauer–Emmett–Teller (BET) specific surface areas and the total pore volumes of the as-prepared HGFs were remarkably higher than that of NGF (Supplementary Table 1). The HGF-III sample displayed the largest BET surface area (524 $m^2 g^{-1}$) and total pore volume (1.27 $cm^3 g^{-1}$), which is likely due to the creation of greater porosity in the bulk sample from excessive etching at higher acid concentrations. Although the specific surface areas of our developed HGFs are substantially lower than the theoretical surface area of 2630 $m^2 g^{-1}$ of an individual graphene sheet[25], they are still comparable to, or greater than those of graphene aerogel (512 $m^2 g^{-1}$)[26], graphene sponge (418 $m^2 g^{-1}$)[27], and graphene nanoplates (480 $m^2 g^{-1}$)[28]. The pore size distributions (PSDs) obtained using the Barrett–Joyner–Halenda (BJH) method revealed that most of the pore volume was contributed by pores of diameter less than 10 nm (Supplementary Fig. 4), with a more prominent pore size distribution in the range of 3–4 nm, implying the presence of narrow mesopores in the basal plane of all the HGFs. While the surface area and total pore volume of the HGFs increased considerably on increasing the volume of acid to the GO precursor, the BJH pore size decreased on increasing the GO/HNO_3 ratio from 1/3 to 1/6 (Supplementary Table 1), leading to a more compact structure for HGF-II. However, further increase in HNO_3 levels yielded HGFs with larger holes, as was evident from the shift of the PSD maxima from 3.29 nm for HGF-II to 3.74 nm for HGF-III. This finding is also consistent with the variations in the I_D/I_G ratio of the samples, suggesting that the degree of etching and the concomitant porosity of the frameworks can be conveniently tuned by the proportion of GO to HNO_3.

Wettability of the HGFs was also quantified by measuring their water contact angles (Supplementary Fig. 5). Small contact angles (<90°) correspond to high surface wettability (hydrophilic), while large contact angles (>90°) correspond to low surface wettability (hydrophobic)[29]. As can be seen from Supplementary Fig. 5, the HGFs exhibited poor wetting with water contact angle greater than 130°. The strong hydrophobicity can be attributed to the surface roughness induced by the morphology of HGFs.

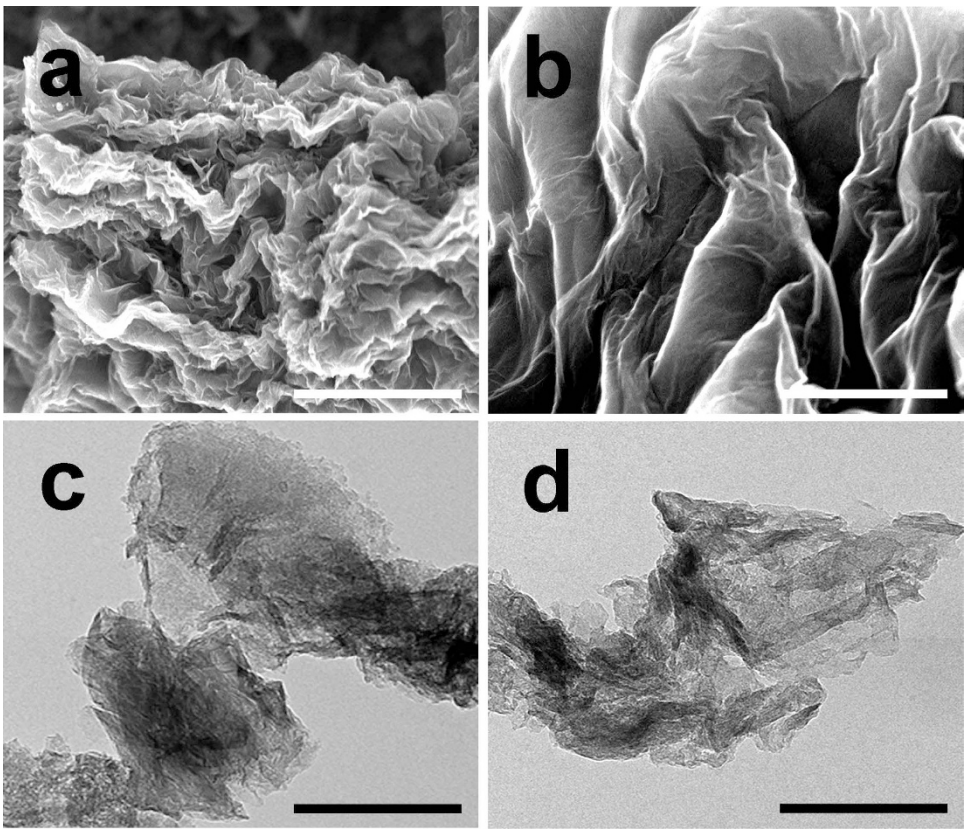

Figure 3. Morphological characterization of HGFs. FESEM images of (**a**) HGF-II and (**b**) NGF. (**c,d**) TEM images of HGF-II. The scale bars in (**a–b**), (**c**) and (**d**) represent 1 μm, 100 nm and 50 nm, respectively.

CO_2 adsorption performance. The efficacy of the synthesized HGF samples for post-combustion CO_2 capture applications was evaluated by measuring their low-pressure CO_2 adsorption capacity using a volumetric gas adsorption apparatus. Under identical experimental conditions, the HGFs exhibited considerably improved CO_2 adsorption in comparison with their non-holey counterpart (Fig. 4a). The CO_2 adsorption capacity of the former (*ca.* 2.11 mmol g^{-1}) was about 3.3 times that of the latter (*ca.* 0.63 mmol g^{-1}) due to the presence of small slit-pores. The adsorption of some amount of CO_2 on NGF could be attributed to the voids between the graphene sheets, generated by the layer-by-layer self-assembly during thermal annealing. In addition, a steep rise in the adsorption capacity at pressure <0.2 bar was found for all the HGFs. The interconnected platelet structure with small mesopores caused more efficient CO_2 diffusion and provided enough space to avoid the steric hindrance effect[30]. As a result, the entire volume of pores in HGFs was readily accessible. Furthermore, no distinct plateau was noticed in the isotherms for the pressure range investigated, indicating that the samples can adsorb greater volume of CO_2 at higher pressure. However, the CO_2 adsorption capacity did not show any apparent correlation with the specific surface area, or pore volume of the HGFs. Notably, the equilibrium CO_2 uptake at 0 °C and 1 bar increased in the following order: HGF-I (1.62 mmol g^{-1}) $<$ HGF-III (1.87 mmol g^{-1}) $<$ HGF-II (2.11 mmol g^{-1}). Even though HGF-III showed the highest BET surface area and total pore volume, the HGF-II material gave the best performance probably because of its smallest mesopore size among all the samples. The contribution of smaller pores in low-pressure CO_2 adsorption is also well-documented in the literature[31]. Moreover, the CO_2 adsorption in HGF-II is better than or comparable to other graphene-based materials at similar temperature and pressure conditions (Supplementary Table 2). Therefore, further CO_2 adsorption studies under flue-gas-like conditions were conducted using the HGF-II sample (Supplementary Fig. 6). A CO_2 partial pressure of 0.15 bar was considered as the representative value for post-combustion carbon capture from flue gas[7]. When adsorption temperature was increased from 0 °C to 25 °C, the amounts of CO_2 adsorbed on HGF-II decreased by 41% at 0.15 bar (0.91 mmol g^{-1} at 0 °C vs. 0.53 mmol g^{-1} at 25 °C), and 34% at 1 bar (2.11 mmol g^{-1} at 0 °C vs. 1.40 mmol g^{-1} at 25 °C). This uptake is, however, higher than the value of 0.37 mmol g^{-1} at 0.15 bar and 30 °C obtained for zeolite[32], 0.11 mmol g^{-1} at 0.15 bar and 25 °C measured for a metal organic framework (MOF)[33], and is comparable to the recently reported value of ~0.55 mmol g^{-1} for activated carbons at 0.15 bar and 25 °C[34]. Further reduction in CO_2 uptake at 50 °C is likely associated with the exothermicity of the adsorption process. Nevertheless, the adsorbed amounts of CO_2 still remain to be 0.34 mmol g^{-1} and 1.02 mmol g^{-1} at 0.15 bar and 1 bar, respectively. Additionally, there was no distinct hysteresis between the CO_2 adsorption and desorption branches (Supplementary Fig. 7). This observation supports the conclusion that HGF-II could be potentially applicable for capturing CO_2 from coal-fired power plant emissions, because near-complete regeneration of the fairly good amount of CO_2 adsorbed was possible for subsequent sequestration or utilization.

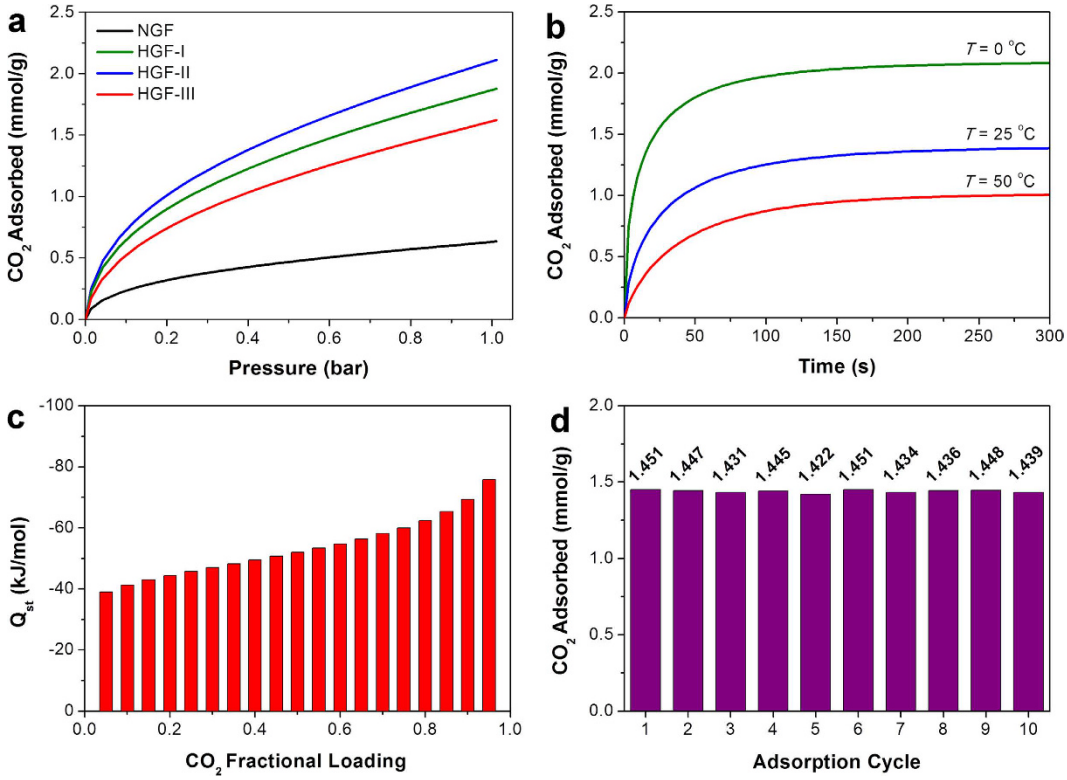

Figure 4. CO_2 adsorption performance of HGFs. (**a**) Pure component CO_2 adsorption isotherms of NGF and HGFs at standard temperature and pressure (0 °C and 1 bar). (**b**) CO_2 adsorption kinetics of HGF-II at different temperatures. (**c**) Calculated isosteric heat of adsorption for HGF-II as function of CO_2 loading. (**d**) Cyclic CO_2 adsorption performance of HGF-II at 25 °C.

The measured pure component isotherm data for CO_2 on HGF-II were fitted with the Toth model[35] to elucidate the underlying adsorption mechanism. The fitted isotherm constants are listed in Supplementary Table 3 while the Supplementary Fig. 8 presents a comparison of CO_2 loadings in HGF-II with the isotherm fits. The goodness-of-fit of the Toth model over the entire pressure and temperature range indicates that CO_2 molecules were adsorbed on HGF-II in multimolecular layers because of the high degree of adsorbent surface heterogeneity. This implies that the adsorption space can accommodate more than one layer of molecules and not all adsorbed molecules are in contact with the surface layer of the adsorbent[36]. Some type of lateral interactions also takes place between the adsorbed molecules[37]. Moreover, the heat evolved during adsorption (i.e., heat of adsorption) is of the same order of magnitude as physical adsorption (5–40 kJ mol^{-1})[38], suggesting that CO_2 was strongly physi-sorbed onto HGF-II essentially through van der Waals forces (also known as dispersion-repulsion forces) and electrostatic forces (also known as Coulombic interactions), arising mainly from quadrupole-quadrupole interactions between CO_2 and the defective graphene surface[39].

Since a typical adsorption cycle in a large-scale commercial CO_2 capture facility will likely be on the order of minutes, the consideration of the rate of adsorption is also very important when evaluating the performance of any new solid CO_2 adsorbent[40]. Indeed, a rapid adsorption will ensure fast cycling times, thereby reducing equipment size and allowing for efficient utilization of the adsorbent[41]. Figure 4b presents the kinetic curves for the HGF-II material at 0, 25 and 50 °C. It can be seen that CO_2 uptake occurred at high adsorption rates, with more than 95% of CO_2 being adsorbed within 3 min, over the range of temperature investigated. The potentially fast adsorption was the outcome of fewer diffusion limitations owing to the narrow mesoporosity of the sample. These results clearly indicate that HGF-II can effectively separate CO_2 from flue gases while operating with very short adsorption/desorption cycle times, which would in turn be economically advantageous for commercial deployment.

As flue gas streams emanating from post-combustion coal-fired power plants contain relatively low concentrations of CO_2 (15%) and large quantities of N_2 (75%)[42], a potential CO_2 capture adsorbent must also be capable of selectively adsorbing the CO_2 component of the gas mixture, such that only pure CO_2 is captured and subjected to sequestration[43]. In fact, the purity of the recovered CO_2 has a significant impact on the technical feasibility of developing an adequate transport and storage infrastructure[44] and is, therefore, critical to CCUS economics. Thus, in this study, the single-component adsorption isotherm for N_2 was measured and compared with the experimental CO_2 isotherm data to evaluate the adsorption selectivity for CO_2 over N_2 (Supplementary Fig. 9). On a gravimetric basis, HGF-II could adsorb about 29 times more CO_2 than N_2 at 25 °C and 1 bar. The high selectivity is a consequence of the exceptionally large polarizability and quadrupole moment of CO_2 (29.11×10^{-25} cm^{-3} and 4.30×10^{-26} esu^{-1} cm^{-1}, respectively) than N_2 (17.40×10^{-25} cm^{-3} and 1.52×10^{-26} esu^{-1} cm^{-1},

respectively)[45]. Because the combustion of coal in air generates flue gas with a total pressure of approximately 1 bar, the selectivity calculation for CO_2 over N_2 is best performed using the adsorption capacities at pressures of approximately 0.15 bar for CO_2 and 0.75 bar for N_2 as follows[43]:

$$S = \frac{q_{CO_2}/q_{N_2}}{P_{CO_2} / P_{N_2}} \quad (1)$$

where S is the selectivity factor, and, q_{CO_2} and q_{N_2} are the amount of CO_2 and N_2 adsorbed at their respective equilibrium partial pressures P_{CO_2} and P_{N_2}. The purity of the captured CO_2 can be then determined from the expression[46]:

$$\text{Purity } (\%) = \frac{q_{CO_2}}{q_{CO_2} + q_{N_2}} \times 100 \quad (2)$$

Attractively, HGF-II exhibited an excellent flue gas normalized CO_2/N_2 selectivity of 70, suggesting that high-purity CO_2 (93.34%) could be recovered from coal-fired dry flue gas. This would in turn enable economic compression, transportation and storage/utilization, and also reduce the costs of installing and operating CCUS systems at power plants. Noticeably, the CO_2/N_2 selectivity as well as the purity of the captured CO_2 for HGF-II is considerably higher than that of several well-known porous solid CO_2 adsorbents (Supplementary Table 4), particularly activated carbons, at pressures and temperatures relevant to practical post-combustion carbon capture. These findings further highlight the suitability of HGF-II as an excellent alternative for the efficient recovery of CO_2 from flue gases emitted by coal-burning power stations.

Quantification of the isosteric heat of adsorption (Q_{st}) is also important for the practical design of an adsorption-based CO_2 capture unit. It governs the local changes in the adsorbent temperature inside an adsorption column during the adsorption/desorption process, which in turn influences the local adsorption equilibria and kinetics, ultimately dictating the overall gas separation efficiency[47]. A moderately high Q_{st} ensures both efficient CO_2 capture and subsequent facile desorption to regenerate the adsorbents[42]. In the present study, the isosteric heat of adsorption of pure CO_2 on HGF-II was determined from the van't Hoff equation by using the temperature-dependent Toth isotherm parameters[48]. At the limit of zero coverage, the isosteric heat of adsorption corresponds to the molar enthalpy of adsorption. This initial Q_{st} of –30.78 kJ mol^{-1} compares well with the previously reported data for pillared graphene frameworks[49], and is lower than those of zeolites[50,51], activated carbons[52,53], and MOFs[54,55]. Additionally, the zero-coverage Q_{st} value at the borderline of strong physisorption and weak chemisorption (*ca.* 25–50 kJ mol^{-1})[56] is likely to afford a lower energy penalty for regenerating the spent HGF-II adsorbent, which would be of potential benefit for reducing the total energy requirements of post-combustion CO_2 capture. Figure 4c illustrates the variation of Q_{st} as a function of the amount of CO_2 adsorbed for the HGF-II adsorbent. Significant increase in the isosteric heat was observed, particularly at higher CO_2 loadings, reaching a maximum of about –75.89 kJ mol^{-1} close to saturation. This behavior is due to pronounced lateral interactions between the adsorbed CO_2 molecules, as was verified by calculating the interaction energy between the adsorbed CO_2 molecules from the Fowler–Guggenheim model[57]. The interaction energy, turned out to be positive (7.33 kJ mol^{-1}), confirming the existence of attractive intermolecular forces among the adsorbed quadrupolar CO_2 molecules. Hence, with more CO_2 molecules present at higher surface loadings, the Q_{st} values were higher than at lower surface loadings. Similar dependence of the isosteric heats of adsorption on surface coverage was also found in other recent works on CO_2 adsorption by carbonaceous materials[58–60].

To further investigate the practical utility and reliability of HGF-II for post-combustion CO_2 capture applications, cyclic CO_2 adsorption/regeneration experiments were conducted by swinging the pressure between vacuum (<0.01 bar) and 1 bar at 25 °C. As shown in Fig. 4d, the amount of CO_2 uptake by HGF-II remained virtually constant with no deterioration in the adsorption capacity even after ten adsorption/regeneration cycles. In addition, the regenerated HGF-II produced similar bands in the FTIR spectrum to those previously observed before the adsorption measurements (Supplementary Fig. 10). It, therefore, appears that the adsorbed CO_2 molecules could be effectively desorbed without destroying the intrinsic structure of the adsorbent during the regeneration step, displaying the stability of our developed HGF-II material for prolonged cyclic operation in CCUS units.

Discussion

We have successfully demonstrated a simple and scalable method to prepare hydrophobic HGFs with superior CO_2 adsorption properties, through acid etching of GO followed by its thermal annealing and self-assembly into 3D interconnected network structure. Our developed HGF materials have several unique features to deliver a high-performance in CO_2 capture applications. First, the graphene sheets in our HGFs are highly crumpled and interconnected to prevent them from face-to-face aggregation and to maintain a highly porous 3D network structure, hence providing a large accessible surface area (497 m^2 g^{-1}) and more "space" (1.22 cm^3 g^{-1}) for adsorbing and storing CO_2. Second, the nanopores in the HGFs have dimensions in the narrow mesopore range, indicating a low-resistant pathway for the diffusion of CO_2 molecules in the frameworks. Last, the HGFs are extremely hydrophobic (water contact angle >130°) due to their surface roughness and porosity, thus avoiding the co-adsorption of moisture while retaining a high adsorption capacity for CO_2 under flue gas conditions. This also represents a conspicuous improvement over zeolites, which are essentially hydrophilic, as well as MOFs, in which the metal–ligand bond is susceptible to hydrolysis and can lead to the collapse of the framework structure upon contact with moist flue gas[43]. Consequently, our HGFs maintained a maximum adsorption uptake of up to 2.11 mmol g^{-1} at 1 bar of dry CO_2. While recent research studies on CO_2 adsorption have focused extensively on achieving ever higher equilibrium adsorption capacities with little or no attention to adsorption kinetics[61], we have investigated

the rate of CO_2 uptake in detail. This is because a high equilibrium uptake does not necessarily translate to a better cyclic adsorption performance as it leads to a longer breakthrough time[61], which in turn implies a smaller number of cycles for the same gas throughput. Such a possibility arises because switching from adsorption to desorption is carried out when the outlet concentration increases to a certain fraction of the feed concentration[61]. Therefore, although some zeolites and many MOFs exhibit higher CO_2 adsorption capacity than our developed HGF adsorbent, their long breakthrough time is likely to result in extended adsorption periods as well as a reduction of the operating efficiency, ultimately compromising the overall productivity and economics of the CO_2 capture process. In contrast, the moderate CO_2 capture capacity of our HGFs together with their rapid kinetics suggests that CO_2 can be effectively separated from flue gas streams while operating with short adsorption cycle times. This attribute would indeed be beneficial for practical industrial applications. Moreover, the adsorption capacity and the structural integrity of HGFs were preserved through multiple adsorption/desorption cycles, demonstrating the stability of these holey graphene macrostructures for long-term cyclic operation. Furthermore, our comparison of CO_2 over N_2 selectivity for various adsorbents under conditions representative of those encountered in coal-fired power plants, reveals the exceptionally superior performance of our HGFs in removing CO_2 from post-combustion flue gas mixtures. The desorbed CO_2 concentration could reach above 93%, which is economically advantageous for subsequent utilization as a feedstock in the chemical industry or permanent storage in deep underground geological formations. Most importantly, the energy input required to regenerate the spent HGFs is low as inferred from the moderate initial isosteric heat of –30.78 kJ mol^{-1}, reflecting an energy-efficient CO_2 adsorbent. Nevertheless, flue gases from power plants also contain other trace combustion by-products (such as CO, NO_X, and SO_X) which may affect the CO_2/N_2 separation performance through competitive adsorption. Hence, further investigations need to be conducted with simulated flue gas mixtures for fully evaluating the effectiveness of our developed HGFs for deployment within real-world CO_2 capture systems.

Methods

Materials. Graphite powder (<20 μm) was purchased from Sigma-Aldrich and used as received. Sulfuric acid (H_2SO_4, 98 wt.%, Merck), nitric acid (HNO_3, 69 wt.%, Honeywell), phosphoric acid (H_3PO_4, 85 wt.%, J.T. Baker), potassium permanganate ($KMnO_4$, Acros Organics), hydrogen peroxide (H_2O_2, 30 wt.%, Sigma-Aldrich), and hydrazine hydrate (N_2H_4, 50–60 wt.%, Sigma-Aldrich) were used as available from the supplier without any further purification.

Synthesis of GO. GO was prepared from natural graphite powder by an improved Hummer's method. In brief, a 9:1 mixture of concentrated H_2SO_4/H_3PO_4 (360:40 mL) was added to a mixture of graphite powder (3 g, 1 wt. equiv.) and $KMnO_4$ (18 g, 6 wt. equiv.), producing a slight exotherm to 35–40 °C. The reaction mixture was further heated to 50 °C and stirred for 12 h. It was then cooled to room temperature and poured onto ice (~400 mL) with 3 mL H_2O_2. Finally, the mixture was centrifuged and the supernatant was decanted away. The remaining solid material was rinsed repeatedly with deionized water until the pH of the solution was neutral. After filtration and drying in air at room temperature, GO was obtained.

Synthesis of HGO. HGO was synthesized through chemical etching of GO with HNO_3. Typically, a weighed amount of GO was suspended in deionized water (10 mL). The resulting inhomogeneous yellow-brown dispersion was then vigorously stirred until a homogeneous solution was obtained. To this dispersion, a desired amount of 69 wt.% concentrated HNO_3 was added under stirring. The mixture was then sonicated in an Elmasonic S 60 H ultrasonic bath (550 W, 37 kHz) (Elma Schmidbauer GmbH, Germany) at room temperature for 1 h. Following sonication, the mixture was allowed to settle at room temperature for an hour, after which the solid was recovered by centrifugation, repeatedly washed with deionized water to neutrality, and finally dried in air. Three different concentrations of HNO_3 were tested, corresponding to a GO suspension/HNO_3 volume ratio of 1/3 (mL/mL) (I), 1/6 (mL/mL) (II) and 1/9 (mL/mL) (III). Accordingly, the resulting materials were labeled as HGO-I, HGO-II and HGO-III, respectively.

Synthesis of HGFs. HGFs were prepared according to the following procedure. The as-prepared HGO was first loaded on a ceramic boat and placed at the center of a horizontal tube furnace (TMH12, Elite Thermal Systems Ltd., UK). The system was then purged with N_2 (500 mL min^{-1}) for 10 min to flush out the air in the tube. After that, the sample was annealed at 500 °C (with a ramp rate of 5 °C min^{-1}) under the N_2 atmosphere for 30 min. The sample was then left to cool naturally to room temperature in the furnace. Depending on the HGO precursor, the materials thus obtained were denoted as HGF-I, HGF-II, and HGF-III, respectively. For comparison, NGFs were synthesized from GO using the same procedure but without any acid treatment.

Characterization. Wide angle XRD patterns were recorded on a Bruker D8 ADVANCE (Bruker Co., Germany) X-ray diffractometer equipped with Ni-filtered Cu Kα radiation ($\lambda = 0.15$ nm) operating at 40 kV and 40 mA. XPS data were acquired using a VG ESCA 220i-XL imaging system (Thermo VG Scientific Ltd., UK). Monochromatic Al Kα X-ray ($h\nu = 1486$ eV) was employed for analysis with a photoelectron take-off angle of 90° to the surface plane. The analysis area was approximately 700 mm in diameter while the maximum analysis depth was in the range of 4–8 nm. FTIR spectra were collected on a Varian Excalibur 3100 FTIR spectrometer (Varian Inc., USA) with a spectral resolution of 2 cm^{-1}. Raman spectra were recorded on a RM 2000 microscopic confocal Raman spectrometer (Renishaw PLC, UK) using a 514 nm laser beam. FESEM was performed on a JEOL JSM-6700F (JEOL Ltd., Japan) field emission microscope operated at an electron accelerating voltage of 15 kV. The samples were mounted on an aluminium stub with carbon adhesive tape and coated with a thin layer of platinum under high vacuum (10^{-3}–10^{-7} Mbar) conditions using a Hitachi E-1030 ion sputter (Hitachi Co. Ltd., Japan) before the FESEM analysis. TEM was carried out on a JEOL JEM 2010F (JEOL Ltd., Japan) transmission electron microscope operated at 200 keV. For TEM measurements, the samples were ultrasonicated in ethanol to form a homogeneous

suspension, dropped on a 200 mesh copper TEM grid coated with a thin amorphous carbon film, and then allowed to dry in air. The textural characteristics were quantified by measuring the N_2 adsorption/desorption isotherms at −196 °C in a Micromeritics ASAP 2020 surface area and porosity analyzer (Micromeritics Instrument Co., USA). All samples were outgassed at 150 °C under vacuum for 1 h prior to the N_2 adsorption measurements. Dynamic water contact angle measurements were performed at room temperature (23 °C) with deionized water using a contact angle measurement setup equipped with a camera (VCA optima, AST Products Inc., USA). Before the measurements, all the samples were dried at 120 °C for 24 h. The dried samples were then pressed between two glass slides that had been previously rinsed with absolute ethanol and dried with a stream of N_2 gas. After removing the upper slide, the exposed sample surface was used for conducting the contact angle measurements. The reported contact angle for each sample is the average of at least three independent measurements.

Gas adsorption measurements. CO_2 adsorption equilibria of the as-prepared materials were measured volumetrically in a Micromeritics ASAP 2020 adsorption apparatus (Micromeritics Instrument Co., USA) at three different temperatures (0, 25 and 50 °C) and pressures of up to 1 bar. The adsorption temperature was controlled by using a Dewar bottle with a circulating jacket connected to a thermostatic bath utilizing water as the coolant. About 100 mg of adsorbent sample was used for the adsorption studies. Before each adsorption experiment, all the samples were degassed at 150 °C under vacuum for 1 h to desorb any moisture and organics. The CO_2 adsorption kinetics (adsorption amount as a function of time) was also measured in the Micromeritics ASAP 2020 system using a built-in function ("Rate of Adsorption") at the same time when the adsorption equilibrium data were collected. The change in gas pressure and adsorption volume with time, after the CO_2–reservoir was connected to the sample chamber, was first registered and then converted into transient adsorption uptakes to generate the adsorption kinetics. The equilibrium adsorption amount was considered as the final adsorption uptake at the terminal pressure and temperature. N_2 adsorption isotherms at 25 °C were also recorded using an identical procedure. Ultra high purity (99.9%) grade gas sources were used throughout the study.

References

1. Leung, D. Y. C., Caramanna, G. & Maroto-Valer, M. M. An overview of current status of carbon dioxide capture and storage technologies. *Renew. Sust. Energ. Rev.* **39,** 426–443 (2014).
2. Wang, J. *et al.* Recent advances in solid sorbents for CO_2 capture and new development trends. *Energy Environ. Sci.* **7,** 3478–3518 (2014).
3. Kemper, J. Biomass and carbon dioxide capture and storage: a review. *Int. J. Greenh. Gas Con.* **40,** 401–430 (2015).
4. Markewitz, P. *et al.* Worldwide innovations in the development of carbon capture technologies and the utilization of CO_2. *Energy Environ. Sci.* **5,** 7281–7305 (2012).
5. von der Assen, N., Voll, P., Peters, M. & Bardow, A. Life cycle assessment of CO_2 capture and utilization: a tutorial review. *Chem. Soc. Rev.* **43,** 7982–7994.
6. Cue´llar-Franca, R. M. & Azapagic, A. Carbon capture, storage and utilisation technologies: A critical analysis and comparison of their life cycle environmental impacts. *J. CO_2 Util.* **9,** 82–102.
7. Balasubramanian, R. & Chowdhury, S. Recent advances and progress in the development of graphene-based adsorbents for CO_2 capture. *J. Mater. Chem. A* **3,** 21968–21989 (2015).
8. Jin, Y., Hawkins, S. C., Huynh, C. P. & Su, S. Carbon nanotube modified carbon composite monoliths as superior adsorbents for carbon dioxide capture. *Energy Environ. Sci.* **6,** 2591–2596 (2013).
9. Wu, Z.-S. *et al.* Three-dimensional graphene-based macro- and mesoporous frameworks for high-performance electrochemical capacitive energy storage. *J. Am. Chem. Soc.* **134,** 19532–19535 (2012).
10. Jiang, L. & Fan, Z. Design of advanced porous graphene materials: from graphene nanomesh to 3D architectures. *Nanoscale* **6,** 1922–1945 (2014).
11. Mao, S., Lu, G. & Chen, J. Three-dimensional graphene-based composites for energy applications. *Nanoscale* **7,** 6294–6943 (2015).
12. Yan, Z. *et al.* Progress in the preparation and application of three-dimensional graphene-based porous nanocomposites. *Nanoscale* **7,** 5563–5577 (2015).
13. Sui, Z.-Y. & Han, B.-H. Effect of surface chemistry and textural properties on carbon dioxide uptake in hydrothermally reduced graphene oxide. *Carbon* **82,** 590–598 (2015).
14. Mi, X. *et al.* Preparation of graphene oxide aerogel and its adsorption for Cu^{2+} ions. *Carbon* **50,** 4856–4864 (2012).
15. Dresselhaus, M. S., Jorio, A., Hofmann, M., Dresselhaus, G. & Saito, R. Perspectives on carbon nanotubes and graphene Raman spectroscopy. *Nano Lett.* **10,** 751–758 (2010).
16. Pimenta, M. A. *et al.* Studying disorder in graphite-based systems by Raman spectroscopy. *Phys. Chem. Chem. Phys.* **9,** 1276–1291 (2007).
17. Moon, I. K., Lee, J., Ruoff, R. S. & Lee, H. Reduced graphene oxide by chemical graphitization. *Nat. Commun.* **1,** 73 (2010).
18. Han, X. *et al.* Scalable holey graphene synthesis and dense electrode fabrication toward high-performance ultracapacitors. *ACS Nano* **8,** 8255–8265 (2014).
19. Xu, Y. *et al.* Solution processable holey-graphene oxide and its derived macrostuctures for high-performance supercapacitors. *Nano Lett.* **15,** 4605–4610 (2015).
20. Han, T. H., Huang, Y.-K., Tan, A. T. L., Dravid, V. P. & Huang, J. Steam etched porous graphene oxide network for chemical sensing. *J. Am. Chem. Soc.* **133,** 15264–15267 (2011).
21. Xu, Y. *et al.* Holey graphene frameworks for highly efficient capacitive energy storage. *Nat. Commun.* **5,** 4554 (2014).
22. Ren, L. *et al.* 3D hierarchical porous graphene aerogel with tunable meso-pores on graphene nanosheets for high-performance energy storage. *Sci. Rep.* **5,** 14229 (2015).
23. Xu, Y., Sheng, K., Li, C. & Shi, G. Self-assembled graphene hydrogel *via* a one-step hydrothermal process. *ACS Nano* **4,** 4324–4330 (2010).
24. Sing, K. S. W. *et al.* Reporting physisorption data for gas/solid systems with special reference to the determination of surface area and porosity. *Pure Appl. Chem.* **57,** 603–619 (1985).
25. Chowdhury, S. & Balasubramanian, R. Recent advances in the use of graphene-family nanoadsorbents for removal of toxic pollutants from wastewater. *Adv. Colloid Interface Sci.* **204,** 35–56 (2014).
26. Zhang, X. *et al.* Mechanically strong and highly conductive graphene aerogel and its use as electrodes for electrochemical power sources. *J. Mater. Chem.* **21,** 6494–6497 (2011).
27. Xu, Z. *et al.* Electrochemical supercapacitor electrodes from sponge-like graphene nanoarchitectures with ultrahigh power density. *J. Phys. Chem. Lett.* **3,** 2928–2933 (2012).

28. Meng, L.-Y. & Park, S.-J. Effect of exfoliation temperature on carbon dioxide capture of graphene nanoplates. *J. Colloid Interface Sci.* **386,** 285–290 (2012).
29. Yuan, Y. & Lee, T. R. In Su*r*face *S*cience Te*chniques* (eds Bracco, G. & Holst, B.) Ch. 1, 3–34 (Springer, 2013).
30. Zhou, L. *et al.* Highly efficient and reversible CO_2 adsorption by amine-grafted platelet SBA-15 with expanded pore diameters and short mesochannels. *Green Chem.* **16,** 4009–4016 (2014).
31. Presser, V., McDonough, J., Yeon, S.-H. & Gogotsi, Y. Effect of pore size on carbon dioxide sorption by carbide derived carbon. *Energy Environ. Sci.* **4,** 3059–3066 (2011).
32. Pham, T. D., Xiong, R., Sandler, S. I. & Lobo, R. F. Experimental and computational studies on the adsorption of CO_2 and N_2 on pure silica zeolites. *Micropor. Mesopor. Mater*. **185,** 157–166 (2014).
33. McEwen, J., Hayman, J.-D. & Yazaydin, A. O. A comparative study of CO_2, CH_4 and N_2 adsorption in ZIF-8, zeolite-13X and BPL activated carbon. *Chem. Phys*. **412,** 72–76 (2013).
34. Tseng, R.-L., Wu, F.-C. & Juang, R.-S. Adsorption of CO_2 at atmospheric pressure on activated carbons prepared from melamine-modified phenol-formaldehyde resins. *Sep. Purif. Technol.* **140,** 53–60 (2015).
35. Chowdhury, S., Parshetti, G. K. & Balasubramanian, R. Post-combustion CO_2 capture using mesoporous TiO_2/graphene oxide nanocomposites. *Chem. Eng. J*. **263,** 374–384 (2015).
36. Burwell, R. L. Manual of symbols and terminology for physicochemical quantities and units, appendix II: Definitions, terminology and symbols in colloid and surface chemistry. *Pure Appl. Chem.* **31,** 577–638 (1972).
37. Al-Muhtaseb, S. A. & Ritter, J. A. Roles of surface heterogeneity and lateral interactions on the isosteric heat of adsorption and adsorbed phase heat capacity. *J. Phys. Chem. B* **103,** 2467–2479 (1999).
38. Creamer, A. E. & Gao, B. *Carbon Dioxide Capture: An Effective Way to Combat Global Warming* (Springer, 2015).
39. Liu, Y. & Wilcox, J. Effects of surface heterogeneity on the adsorption of CO_2 in microporous carbons. *Environ. Sci. Technol.* **46,** 1940–1947 (2012).
40. Bollini, P., Didas, S. A. & Jones, C. W. Amine-oxide hybrid materials for acid gas separations. *J. Mater. Chem. A* **21,** 15100–15120 (2011).
41. Fan, Y. *et al.* Evaluation of CO_2 adsorption dynamics of polymer/silica supported poly(ethylenimine) hollow fiber sorbents in rapid temperature swing adsorption. *Int. J. Greenh. Gas Con.* **21,** 61–71 (2014).
42. Liu, Y., Wang, Z. U. & Zhou, H.-C. Recent advances in carbon dioxide capture with metal-organic frameworks. *Greenhouse Gas Sci. Technol*. **2,** 239–259 (2012).
43. Sumida, K. *et al.* Carbon dioxide capture in metal-organic frameworks. *Chem. Rev.* **112,** 724–781 (2012).
44. Sass, B. M. *et al.* Considerations for treating impurities in oxy-combustion flue gas prior to sequestration. *Energy Procedia* **1,** 535–542 (2009).
45. Li, J.-R., Kuppler, R. J. & Zhou, H.-C. Selective gas adsorption and separation in metal-organic frameworks. *Chem. Soc. Rev.* **38,** 1477–1504 (2009).
46. Lee, W. R. *et al.* Exceptional CO_2 working capacity in a heterodiamine-grafted metal-organic framework. *Chem. Sci*. **6,** 3697–3705 (2015).
47. Cao, D. V. & Sircar, S. Heats of adsorption of pure SF_6 and CO_2 on silicalite pellets with alumina binder. *Ind. Eng. Chem. Res.* **40,** 156–162 (2001).
48. Duong, D. D. *Adsorption Analysis: Equilibria and Kinetics* (Imperial College Press, 1998).
49. Kumar, R., Suresh, V. M., Maji, T. K. & Rao, C. N. R. Porous graphene frameworks pillared by organic linkers with tunable surface area and gas storage properties. *Chem. Commun.* **50,** 2015–2017 (2014).
50. Yang, S.-T., Kim, J. & Ahn, W.-S. CO_2 adsorption over ion-exchanged zeolite beta with alkali and alkaline earth metal ions. *Micropor. Mesopor. Mat.* **135,** 90–94 (2010).
51. Zukal, A. *et al.* Combined volumetric, infrared spectroscopic and theoretical investigation of CO_2 adsorption on Na-A zeolite. *Micropor. Mesopor. Mat.* **146,** 97–105 (2011).
52. Yang, Z., Xia, Y. & Zhu, Y. Preparation and gases storage capacities of N-doped porous activated carbon materials derived from mesoporous polymer. *Mater. Chem. Phys.* **141,** 318–323 (2013).
53. Shafeeyan, M. S., Wan Daud, W. M. A., Shamiri, A. & Aghamohammadi, N. Adsorption equilibrium of carbon dioxide on ammonia-modified activated carbon. *Chem. Eng. Res. Des.* **104,** 42–52 (2015).
54. An, J. & Rosi, N. L. Tuning MOF CO_2 adsorption properties via cation exchange. *J. Am. Chem. Soc.* **132,** 5578–5579 (2010).
55. McDonald, T. M., D'Alessandro, D. M., Krishna, R. & Long, J. R. Enhanced carbon dioxide capture upon incorporation of N,N′-dimethylethylenediamine in the metal–organic framework CuBTTri. *Chem. Sci*. **2,** 2022–2028 (2011).
56. Mohanty, P., Kull, L. D. & Landskron, K. Porous covalent electron-rich organonitridic frameworks as highly selective sorbents for methane and carbon dioxide. *Nat. Commun.* **2,** 401 (2011).
57. Hamdaoui, O. & Naffrechoux, E. Modeling of adsorption isotherms of phenol and chlorophenols onto granular activated carbon Part I. Two-parameter models and equations allowing determination of thermodynamic parameters. *J. Hazard. Mater.* **147,** 381–394 (2007).
58. Krungleviciute, V., Migone, A. D., Yudasaka, M. & Iijima, S. CO_2 adsorption on dahlia-like carbon nanohorns: isosteric heat and surface area measurements. *J. Phys. Chem. C* **116,** 306–310 (2012).
59. Goel, C., Bhunia, H. & Bajpai, P. K. Development of nitrogen enriched nanostructured carbon adsorbents for CO_2 capture. *J. Environ. Manage.* **162,** 20–29 (2015).
60. Chowdhury, S. & Balasubramanian, R. Highly efficient, rapid and selective CO_2 capture by thermally treated graphene nanosheets. *J. CO_2 Util*. **13,** 50–60 (2016).
61. Bollini, P., Brunelli, N. A., Didas, S. A. & Jones, C. W. Dynamics of CO_2 adsorption on amine adsorbents. 2. Insights into adsorbent design. *Ind. Eng. Chem. Res.* **51,** 15153–15162 (2012).

Acknowledgements

Shamik Chowdhury gratefully acknowledges the financial support provided by the National University of Singapore for his Doctoral study. The authors thank Madam Loy Gek Luan of the Cryo-Electron Microscopy Facility at Center for Bio-imaging Science, Department of Biological Science, National University of Singapore for her technical assistance with TEM. The authors are also thankful to A*STAR's Institute of Materials Research and Engineering (IMRE), Singapore for their technical assistance.

Author Contributions

S.C. and R.B. jointly conceived the study. S.C. organized and performed the experiments, analyzed the data and wrote the manuscript. R.B. designed and supervised the experiments, interpreted the data, and edited the manuscript.

Additional Information

Supplementary information accompanies this paper at http://www.nature.com/srep

Competing financial interests: The authors declare no competing financial interests.

How to cite this article: Chowdhury, S. and Balasubramanian, R. Holey graphene frameworks for highly selective post-combustion carbon capture. *Sci. Rep.* **6**, 21537; doi: 10.1038/srep21537 (2016).